

Abstract

Measurement of total hadronic differential cross sections in the LArIAT experiment

Elena Gramellini

2018

Abstract goes here. Limit 750 words.

Measurement of total hadronic differential cross sections in the LArIAT experiment

A Dissertation
Presented to the Faculty of the Graduate School
of
Yale University
in Candidacy for the Degree of
Doctor of Philosophy

by
Elena Gramellini

Dissertation Director: Bonnie T. Fleming

Date you'll receive your degree

Copyright © 2017 by Elena Gramellini
All rights reserved.

Contents

Acknowledgements	v
0 The theoretical framework	1
0.1 The Standard Model	1
0.2 Neutrinos: tiny cracks in the Standard Model	3
0.2.1 Neutrinos in the Standard Model	3
0.2.2 Neutrino Oscillations	5
0.2.3 Make up of Neutrino Interactions	6
0.3 Beyond the Standard Model	10
0.3.1 Open Questions in Neutrino Physics	10
0.3.2 Towards a more fundamental theory: GUTs	14
0.4 Motivations for Hadronic Cross Sections in Argon	17
0.4.1 Pion-Argon Total Hadronic Cross Section	17
0.4.2 Kaon-Argon Total Hadronic Cross Section	27
1 Liquid Argon Detectors at the Intensity Frontier	32
1.1 The Liquid Argon Time Projection Chamber Technology	32
1.1.1 Time Projection Chamber	32
1.1.2 LArTPC: Principles of Operation	32
1.1.3 Liquid Argon: Ionization Charge	34
1.1.4 Liquid Argon: Scintillation Light	35

1.1.5	Signal processing	39
1.2	The Intensity Frontier Program	39
1.2.1	SBN: Neutrino Interaction and Detection	39
1.2.2	DUNE: Rare Decay Searches	39
1.2.3	Enabling the next generation of discoveries: LArIAT	39

Acknowledgements

A lot of people are awesome, especially you, since you probably agreed to read this when it was a draft.

Chapter 0

The theoretical framework

0.1 The Standard Model

The Standard Model (SM) of particle physics is the most accurate theoretical description of the subatomic world and, in general, one of the most precisely tested theories in the history of physics. The SM describes the strong, electromagnetic and weak interactions among elementary particles in the framework of quantum field theory, accounting for the unification of electromagnetic and weak interactions for energies above the vacuum expectation value (VEV) of the Higgs field. The SM does not describe gravity or general relativity.

The Standard Model is a gauge theory based on the local group of symmetry

$$G_{SM} = SU(3)_C \otimes SU(2)_T \otimes U(1)_Y \quad (1)$$

where the subscripts indicate the conserved charges: the strong charge, or color C, the weak isospin T (or rather its third component T₃) and the hypercharge Y. These quantities can be related to the electric charge Q through the Gell-Mann-Nishijima relation:

$$Q = \frac{Y}{2} + T_3. \quad (2)$$

Generation	I	II	III	T	Y	Q
Leptons	$\begin{pmatrix} \nu_e \\ e \end{pmatrix}_L$	$\begin{pmatrix} \nu_\mu \\ \mu \end{pmatrix}_L$	$\begin{pmatrix} \nu_\tau \\ \tau \end{pmatrix}_L$	$\begin{matrix} 1/2 \\ -1/2 \end{matrix}$	$\begin{matrix} -1 \\ -1 \end{matrix}$	$\begin{matrix} 0 \\ -1 \end{matrix}$
	e_R	μ_R	τ_R	0	-2	1
Quarks	$\begin{pmatrix} u \\ d' \end{pmatrix}_L$	$\begin{pmatrix} c \\ s' \end{pmatrix}_L$	$\begin{pmatrix} t \\ b' \end{pmatrix}_L$	$\begin{matrix} 1/2 \\ -1/2 \end{matrix}$	$\begin{matrix} 1/3 \\ 1/3 \end{matrix}$	$\begin{matrix} 2/3 \\ -1/3 \end{matrix}$
	u_R	c_R	t_R	0	$4/3$	$2/3$
	d'_R	s'_R	b'_R	0	$-2/3$	$-1/3$

Table 1: SM elementary fermions. The subscripts L and R indicate respectively the negative helicity (left-handed) and the positive helicity (right-handed).

In the quantum field framework, the elementary particles correspond to the irreducible representations of the G_{SM} symmetry group. In particular, the particles are divided in two categories, fermions and bosons, according to their spin-statistics. Described by the Fermi-Dirac statistics, fermions have half-integer spin and are sometimes called “matter-particles”. Bosons or “force carriers” have integer spin, follow the Bose-Einstein statistics and mediate the interaction between fermions. The fundamental fermions and their quantum numbers are listed in Tab 1.

Quarks can interact via all three the fundamental forces; they are triplets of $SU(3)_C$, that is they can exist in three different colors: $C = R, G, B$. If one chooses a base where u , c and t quarks are simultaneously eigenstates of both the strong and the weak interactions, the remaining eigenstates are usually written as d , s and b for the strong interaction and d' , s' and b' for the weak interaction, because the latter ones are the result of a Cabibbo rotation on the first ones. Charged leptons interact via the weak and the electromagnetic forces, while neutrinos only interact via the weak force. The gauge group univocally determines the number of gauge bosons that carry the interaction; the gauge bosons correspond to the generators of

the group: eight gluons (g) for the strong interaction, one photon (γ) and three bosons (W^\pm, Z^0) for the electroweak interaction. A gauge theory by itself can not provide a description of massive particles, but it is experimentally well known that most of the elementary particles have non-zero masses. The introduction of massive fields in the Standard Model lagrangian would make the theory non-renormalizable, and - so far - mathematically impossible to handle. This problem is solved in the SM by the introduction of a scalar iso-doublet $\Phi(x)$, the Higgs field, which gives mass to W^\pm and Z^0 gauge bosons through the electroweak symmetry breaking mechanism and to the fermions through Yukawa coupling [?, ?]. The discovery of the Higgs boson in 2012 by the LHC experiments [?, ?] marked the ultimate confirmation of a long history of successful predictions by the SM.

0.2 Neutrinos: tiny cracks in the Standard Model

0.2.1 Neutrinos in the Standard Model

Neutrino were introduced in the SM as left-handed massless Weyl spinors. The Dirac equation of motion

$$(i\gamma^\mu\partial_\mu - m)\psi = 0 \tag{3}$$

for a fermionic field

$$\psi = \psi_L + \psi_R \tag{4}$$

is equivalent to the equations

$$i\gamma^\mu\partial_\mu\psi_L = m\psi_R \tag{5}$$

$$i\gamma^\mu\partial_\mu\psi_R = m\psi_L \tag{6}$$

for the chiral fields ψ_R and ψ_L , whose evolution in space and time is coupled through the mass m . If the fermion is massless, the chiral fields decouple and the

fermion can be described by a single Weyl spinor with two independent components [?]. Pauli initially rejected the description of a physical particle through a single Weyl spinor because of its implication of parity violation. In fact, since the spatial inversion operator throws $\psi_R \leftrightarrow \psi_L$, parity is conserved only if the both the chiral components exist at the same time. For the neutrino introduction in the SM, experiments came in help of the theoretical description. The constraint of parity conservation weakened after Wu's experiment in 1957 [?]. Additionally, there was no experimental indication for massive neutrinos, nor evidence of interaction via the neutrino right-handed component.

The symmetry group $SU(2)_T \otimes U(1)_Y$ is the only group relevant for neutrino interactions. The SM electroweak lagrangian is the most general renormalizable lagrangian invariant under the local symmetry group $SU(2)_T \otimes U(1)_Y$. The lagrangian couples the weak isotopic spin doublets and singlets described in Table 1 with the gauge bosons A_a^μ ($a = 1, 2, 3$) and B^μ , and Higgs doublet $\Phi(x)$:

$$\begin{aligned}
\mathcal{L} = & i \sum_{\alpha=e,\mu,\tau} \bar{L}'_{\alpha L} \not{D} L'_{\alpha L} + i \sum_{\alpha=1,2,3} \bar{Q}'_{\alpha L} \not{D} Q'_{\alpha L} \\
& + i \sum_{\alpha=e,\mu,\tau} \bar{l}'_{\alpha R} \not{D} l'_{\alpha R} + i \sum_{\alpha=d,s,b} \bar{q}'^D_{\alpha R} \not{D} q'^D_{\alpha R} + i \sum_{\alpha=u,c,t} \bar{q}'^U_{\alpha R} \not{D} q'^U_{\alpha R} \\
& - \frac{1}{4} A_{\mu\nu} A^{\mu\nu} - \frac{1}{4} B_{\mu\nu} B^{\mu\nu} \\
& + (D_\rho \Phi)^\dagger (D^\rho \Phi) - \mu^2 \Phi^\dagger \Phi - \lambda (\Phi^\dagger \Phi)^2 \\
& - \sum_{\alpha,\beta=e,\mu,\tau} \left(Y_{\alpha\beta}^n \bar{L}'_{\alpha L} \Phi l'_{\beta R} + Y_{\alpha\beta}^{n*} \bar{l}'_{\beta R} \Phi^\dagger L'_{\alpha L} \right) \\
& - \sum_{\alpha=1,2,3} \sum_{\beta=d,s,b} \left(Y_{\alpha\beta}'^D \bar{Q}'_{\alpha L} \Phi q'^D_{\beta R} + Y_{\alpha\beta}'^{D*} \bar{q}'^D_{\beta R} \Phi^\dagger Q'_{\alpha L} \right) \\
& - \sum_{\alpha=1,2,3} \sum_{\beta=u,c,t} \left(Y_{\alpha\beta}'^U \bar{Q}'_{\alpha L} \tilde{\Phi} q'^U_{\beta R} + Y_{\alpha\beta}'^{U*} \bar{q}'^U_{\beta R} \tilde{\Phi}^\dagger Q'_{\alpha L} \right). \tag{7}
\end{aligned}$$

The first two lines of the lagrangian summarize the kinetic terms for the fermionic

fields and their coupling to the gauge bosons $A_a^{\mu\nu}$, $B^{\mu\nu}$ ¹. The third line describes the kinetic terms and the self-coupling terms of the gauge bosons. The fourth line is the Higgs lagrangian, which results in the spontaneous symmetry breaking. The last three lines describe the Yukawa coupling between fermions and the Higgs field, origin of the fermions' mass.

The coupling between left-handed and right-handed field generates the mass term for fermions. The SM assumes only left-handed components for neutrinos, thus implying zero neutrino mass. Since any linear combination of massless fields results in a massless field, the flavor eigenstates are identical to the mass eigenstates in the SM.

0.2.2 Neutrino Oscillations

The determination of the flavor of a neutrino dynamically arises from the corresponding charged lepton associated in a charge current interaction; for example, a ν_e is a neutrino which produces an e^- , a $\bar{\nu}_\mu$ is a neutrino which produces a μ^+ , *etc.* The neutrino flavor eigenstates $|\nu_\alpha\rangle$, with $\alpha = e, \mu, \tau$, are orthogonal to each other and form a base for the weak interaction matrix.

Overwhelming experimental data show neutrinos change flavor during their propagation [?]. This phenomenon, called “neutrino oscillations”, was predicted first by Bruno Pontecorvo in 1957 [?]. Neutrino oscillations are possible only if the neutrino flavor eigenstate are not identical to the mass eigenstates, thus resulting in the first evidence of physics beyond the Standard Model. A minimal extension of the SM introduces three mass eigenstates, $|\nu_i\rangle$ ($i = 1, 2, 3$), whose mass m_i is well defined. The unitary Pontecorvo-Maki-Nakagawa-Sakata matrix transforms the spinor wave functions (ψ) of each component between the flavor and mass bases as follows

1. In gauge theories the ordinary derivative ∂_μ is substituted with the covariant derivative D_μ . Here $D_\mu = \partial_\mu + igA_\mu \cdot I + ig'B_\mu \frac{Y}{2}$, where I and Y are the $SU(2)_L$ and $U(1)_Y$ generators, respectively.

$$\sum_{\alpha} \psi_{\alpha} |\nu_{\alpha}\rangle = \sum_i \psi_i |\nu_i\rangle, \rightarrow \psi_{\alpha} = U_{PMNS} \psi_i, \quad (8)$$

with

$$U_{PMNS} = \begin{bmatrix} c_{12} & s_{12} & 0 \\ -s_{12} & c_{12} & 0 \\ 0 & 0 & 1 \end{bmatrix} \begin{bmatrix} c_{13} & 0 & s_{13}e^{-i\delta} \\ 0 & 1 & 0 \\ -s_{13}e^{-i\delta} & 0 & c_{13} \end{bmatrix} \begin{bmatrix} 1 & 0 & 0 \\ 0 & c_{23} & s_{23} \\ 0 & -s_{23} & c_{23} \end{bmatrix} \begin{bmatrix} e^{i\alpha_1} & 0 & 0 \\ 0 & e^{i\alpha_2} & 0 \\ 0 & 0 & 1 \end{bmatrix} \quad (9)$$

where c e s stand respectively for cosine and sine of the corresponding mixing angles (θ_{12} , θ_{23} and θ_{13}), δ is the Dirac CP violation phase, α_1 and α_2 is the eventual Majorana CP violation phases. Experimental results on neutrino oscillations are generally reported in terms of the mixing angles and of the squared mass splitting $\Delta m_{ab}^2 = m_a^2 - m_b^2$, where a and b represent the mass eigenstates. A summary of the current status of experimental results, albeit partial, is given in table 2.

Table 2: Summary of experimental results on neutrino oscillation parameters. **ADD CITATIONS**

	Value	Precision	Experiment
θ_{23} Δm_{23}^2	45° $2.5 \cdot 10^{-3} \text{ eV}^2$	9.0% 1.8%	Super Kamiokande, MINOS, Nova, MACRO
θ_{12} Δm_{12}^2	34° $7.4 \cdot 10^{-5} \text{ eV}^2$	5.8% 2.8%	SNO, Gallex, SAGE, KamLAND
θ_{13} Δm_{13}^2	9° $2.5 \cdot 10^{-3} \text{ eV}^2$	4.7% 1.8%	DAYA Bay, RENO

0.2.3 Make up of Neutrino Interactions

All neutrino experiments involving the detection of single neutrinos are concerned with neutrino interactions (and neutrino cross sections) on nuclei. Given the invisible nature of the neutrino, characterizing the products of its interaction is the only

method to a) assess the neutrino presence, b) detect its flavor in case of a charge current interaction and c) eventually reconstruct its energy.

Historically, neutrino interactions with the nucleus in the GeV region are divided into three categories as a function of increasing neutrino energy: quasi elastic (QE), resonant, and deep inelastic (DIS) scattering. All current and forthcoming oscillation experiments live in the 0.1-10 GeV transition region, which encompasses the energy where the QE neutrino-nucleus interaction transitions into resonant scattering and the energy where resonance scattering transitions into DIS. Schematically, neutrino and antineutrino QE charge current scattering refers to the process $\nu_l n \rightarrow l^- p$ and $\bar{\nu}_l p \rightarrow l^+ n$ where a charged lepton and single nucleon are ejected in the elastic interaction, leaving the target nucleus in its ground state. Resonant scattering refers to an inelastic collision producing a nucleon excited state (Δ, N^*) – the resonance, indeed – which then quickly decays, most often to a nucleon and single-pion final state. DIS refers to the head-on collision between the neutrino and a parton inside the nucleon, producing hadronization and subsequent abundant production of mesons and nucleons. In addition to such interactions between the neutrino and a single component of the nucleus, neutrinos can also interact with the nucleus as a whole, albeit more rarely, a well documented process called coherent meson production scattering [?]; the signature of such process is the production of a distinctly forward-scattered single meson final state, most often a pion. This simple picture of neutrino interactions works rather well for scattering off of light nuclear targets, such as the H_2 and D_2 of bubble chamber experiments [?], but the complexity of the nuclear structure for heavier nuclei such as argon complicates this model.

As we will discuss in Chapter 1, the properties of argon make it a good candidate for interacting medium in neutrino experiments; in particular the density of its interaction centers augments the yield of neutrino interactions and allows for relatively compact detectors. Though, the choice of a relatively heavy nuclear target comes at

the cost of enhancing nuclear effects which modify the kinematic and final state of the neutrino interaction products.

Nuclear effects can potentially affect the neutrino event rates, nucleon emission, neutrino energy reconstruction, and the neutrino/antineutrino ratios, carrying deep implications for oscillation experiments. Even in the case of “simple” QE scattering, intra-nuclear hadron rescattering and correlation effects between the target nucleons can cause the ejection of additional nucleons in the final state, modifying the final state kinematics and topology. In case of resonant and DIS scattering, the hadronic interactions of meson and nucleons produced in the decay of the resonance or during hadronization complicate this picture even more. A large source of uncertainty in modeling nuclear effects in neutrino interactions come from mesons interactions (and re-interactions) in the nucleus, e.g., pion re-scattering, charge exchange, and absorption.

A renewed interest for neutrino cross section measurements surged in recent years, along with a lively discussion on the data reporting; the historical method of reporting the neutrino cross section as a function of the neutrino energy or momentum transferred shakes under the weight of its dependency on the chosen nuclear model. On one hand, correcting for nuclear effects in neutrino interaction can introduce unwanted sources of uncertainty and model dependency especially due to the mis-modeling of the meson interactions. On the other, avoiding this correction makes a comparison between neutrino interactions on different target nuclei extremely difficult.

Data on neutrino scattering off many different nuclei are available for both charged current (CC) and neutral current (NC) channels, as summarized in [?]. A summary of the results on QE, resonant and DIS scattering for neutrinos and antineutrinos from accelerators on different target is reported in Figure 1, where the (NUANCE) [?] event generator is used as comparison with the theory.

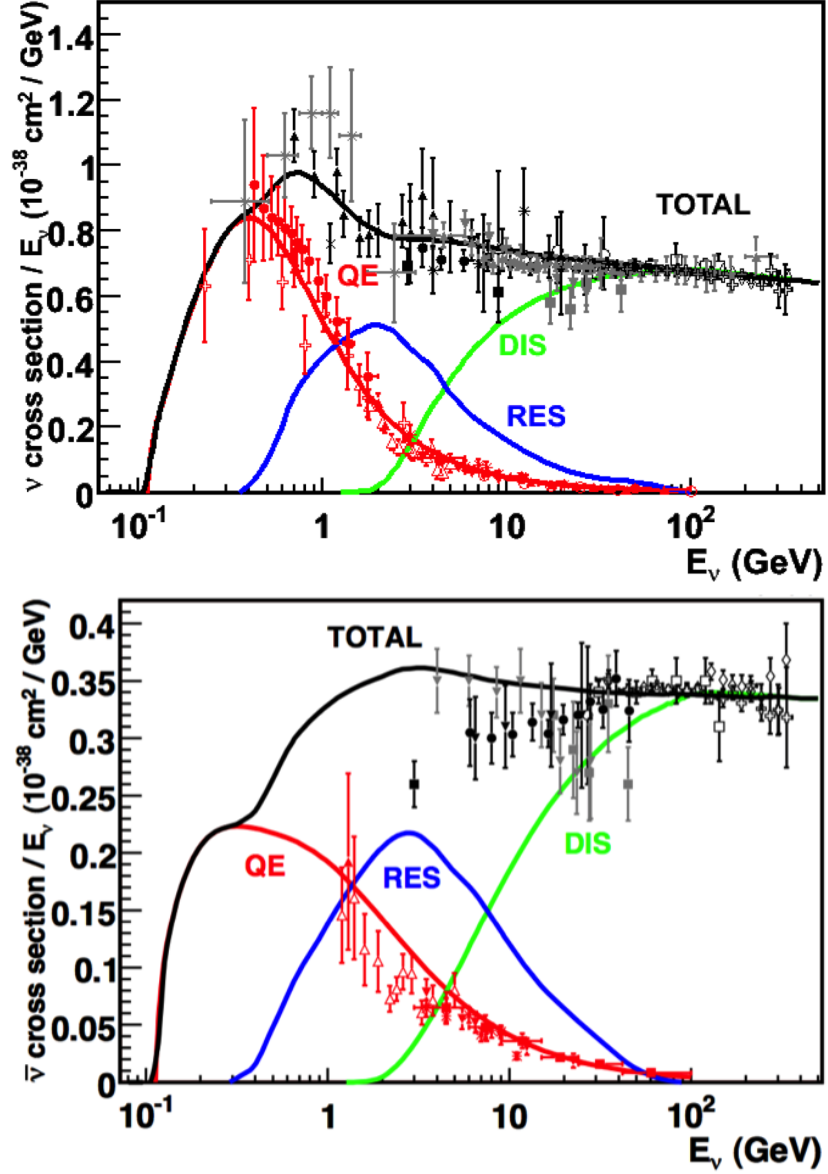


Figure 1: Total neutrino (top) and antineutrino (bottom) CC cross sections per nucleon divided by neutrino energy as a function of energy as reported in [?]. Predictions for the total (black), the QE (red), resonant (blue) and DIS (green) are provided by the NUANCE generator. The quasi-elastic scattering data and predictions have been averaged over neutron and proton targets (isoscalar target).

0.3 Beyond the Standard Model

The discovery of neutrino oscillation and its implication of non-zero neutrino mass mark the beginning of a new, exciting era in neutrino physics: the era of physics Beyond the Standard Model (BSM) at the intensity frontier. We are currently searching for new, deeper theories that can accommodate neutrinos with tiny but non-zero masses, while remaining consistent with the rest of the Standard Model.

0.3.1 Open Questions in Neutrino Physics

On one hand, the last three decades of experiments in neutrino oscillations brought spectacular advancements in the understanding of the oscillations pattern, measuring the neutrino mixing angles and mass splitting with a precision of less than 10%. On the other, it opened the field for a series of questions needing experimental answers.

Sterile neutrinos. Hints to the existence of at least one additional neutrino, in the form of various anomalies, have been puzzling physicists almost from the beginning of neutrino oscillation searches. Originally designed to look for evidence of neutrino oscillation, the Liquid Scintillator Neutrino Detector (LSND) [?] provided a first conflicting result with the Standard Model expectation of only three neutrinos. A second conflicting result has also been provided by the MiniBooNE experiment [?]. The LSND and MiniBooNE ν_e and $\bar{\nu}_e$ appearance results, known as the “LSND and MiniBooNE anomalies” [?, ?, ?], may be interpreted under the assumption of a new right-handed neutrino. The additional neutrino needs to be “sterile”, i.e. needs not to couple with the electroweak force carriers, in order to meet the constraint imposed by the measurement of the width of the Z boson [?]. The new sterile neutrino would mainly be composed of a heavy neutrino ν_4 with mass m_4 such that $m_1, m_2, m_3 \ll m_4$ and $\Delta m^2 = \Delta m_{14}^2 \sim [0.1 - 10] \text{ eV}^2$. The introduction of sterile neutrinos is an appealing line of thinking, since this renormalizable generalization of the SM has the

potential to impact long standing questions in high energy physics and cosmology: light sterile neutrinos are candidates for dark matter particles and there are ideas that the theory could be adjusted to explain the baryon asymmetry of the Universe via leptogenesis [?].

CP Violation In Lepton Sector. The measurement of non-zero value for the oscillation parameter θ_{13} allows the exploration of low-energy CP violation in the lepton sector at neutrino long baseline oscillation experiments, enabling the possibility to measure the Dirac CP-violating phase δ . Exciting theoretical results tie δ directly to the generation of the baryon asymmetry of the Universe at the Grand Unified Theory scale **a couple of cit would be nice**. According to the theoretical model described in [?], for example, leptogenesis can be achieved if $|\sin \theta_{13} \sin \delta| > 0.11$, i.e. $\sin \delta > 0.7$.

The asymmetry in the oscillation probability of neutrinos and antineutrinos is the observable sensitive to the Dirac CP-violating phase δ leveraged in neutrino oscillation experiments. Using the parameterization of the PMNS matrix shown in Equation 9, the difference between the probability of $\nu_e \rightarrow \nu_\mu$ oscillation and the probability of $\bar{\nu}_e \rightarrow \bar{\nu}_\mu$ oscillation can be parametrized as follows [?],

$$P_{\nu_e \rightarrow \nu_\mu} - P_{\bar{\nu}_e \rightarrow \bar{\nu}_\mu} = J \cos \left(\pm \delta - \frac{\Delta_{31} L}{2} \right) \sin \left(\frac{\Delta_{21} L}{2} \right) \sin \left(\frac{\Delta_{31} L}{2} \right) \quad (10)$$

where

$$J = \cos \theta_{13} \sin 2\theta_{13} \sin 2\theta_{12} \sin 2\theta_{23} \quad (11)$$

is the Jarlskog invariant [?], L the neutrino baseline and Δ_{ab} a factor proportional to the sign and magnitude of the mass splitting. From these equations, it is clear how the relative large value of θ_{13} is a happy accident necessary not to completely suppress the sensitivity to CP violation. The equations also show how the sensitivity to δ is tied to the measurement of the least precisely measured mixing angle, θ_{23} (via the $\sin 2\theta_{23}$

term) and to an other unknown quantity, the neutrino “mass hierarchy” (via the Δ_{ab} terms). The precise determination of θ_{23} is often referred as to “the octant problem”. Current experimental results [cite NOVA T2K](#) are consistent with $\theta_{23} = 45^\circ$, which would imply maximal mixing between $\nu_\mu - \nu_\tau$, hinting to an intriguing new symmetry. Therefore, a precise measurement of θ_{23} is of great interest for theoretical models of quark-lepton universality [change cit \[59,84,85,86,87,88\]](#), whose quark and lepton mixing matrices are proportional to the deviation of θ_{23} from 45° .

Neutrino mass hierarchy. The “mass hierarchy” problem refers to the unknown ordering of the value of absolute mass of the neutrino mass eigenstates. Current oscillation experiments are sensitive only to the magnitude of the mass splitting, but not to its sign. [cite hints](#) In a framework where the lightest neutrino mass (arbitrarily) corresponds to the first eigenstate m_1 , it is unknown whether $m_2 - m_1 < m_3 - m_1$ (Normal Hierarchy) or $m_2 - m_1 > m_3 - m_1$ (Inverted Hierarchy). The mass hierarchy affects not only the sensitivity to CP violation searches in long baseline oscillation experiments, but also the sensitivity to determine whether neutrinos are Majorana particles in neutrinoless double beta decay experiments.

Majorana or Dirac? Evidence of neutrino oscillations demands the introduction of a mechanism which can give mass to the neutrinos. This mechanism should possibly also explain why neutrino masses are at least six orders of magnitude lower than the electron mass (the second lightest SM fermion). In a description of neutrinos as Dirac 4-component spinors, the neutrino field acquires mass via the Higgs mechanism as any other fermion of the SM. In this case, the neutrino mass is given by $m_a = \frac{y_a^\nu v}{\sqrt{2}}$, where v is the Higgs VEV and y_a^ν is the Yukawa coupling between the Higgs and the neutrino. The smallness of neutrino masses can only be pinned on a tiny Yukawa coupling which is not justified by the theory.

In 1937, Majorana demonstrated that the introduction of a two components spinor is sufficient to describe a massive fermion [?]. The Dirac equations of motion for

the chiral fields (equations 5 and 6) hold true in the case of two components spinor under the assumption that the chiral components ψ_R and ψ_L are correlated through the charge conjugation matrix \mathcal{C} , $\psi_R = \mathcal{C}\bar{\psi}_L$. Therefore the theory is applicable only to neutral fermions. Neutrinos are the only neutral elementary particles in the SM – the only possible Majorana particle candidate. This theory constructs a neutrino Majorana mass term \mathcal{L}_5 of the following form in the Higgs unitary gauge

$$\mathcal{L}_5 = \frac{1}{2} \frac{gv^2}{\mathcal{M}} \nu_L^T \mathcal{C}^\dagger \nu_L, \quad (12)$$

where g is the coupling coefficient, v the Higgs VEV and \mathcal{M} a constant with the dimension of the mass proportional to the scale of new physics. The \mathcal{L}_5 term would introduce a non-renormalizable term in the lagrangian, since it has dimensions of energy to the fifth power. This is not allowed in the SM lagrangian; however, the existence of such terms is plausible if we consider the SM as an effective theory at low energy, manifestation of the symmetry breaking of a Grand Unified Theory (GUT) at higher energy, and not the definitive theory. The mass term in eq 12 implies the neutrino mass to be $m = \frac{gv^2}{\mathcal{M}}$. The coupling coefficient can be of the order of any other fermion's coupling coefficient, since the smallness of neutrino masses is achieved by the big value of the new physics mass scale alone. This vanilla formulation is the conceptual basis for many flavors of *seesaw mechanism* [?], which we will not discuss here in any detail. However, it is fascinating how the puzzle of the neutrino mass hints to the existence of a deeper and more complete theory.

From a kinematic point of view, Dirac and Majorana neutrinos satisfy the same energy-momentum dispersion relationship. Thus, it is impossible to discern the neutrino nature through kinematic effects such as neutrino oscillations. Neutrinoless double beta decay searches are the most promising way to understand the nature of the neutrino and are therefore subject of great theoretical and experimental interest.

Observation of the lepton number violating process $0\nu\beta\beta$ would imply neutrinos have a Majorana component. Depending on the mass hierarchy, the theory also predicts $0\nu\beta\beta$ exclusion regions and confirmation of the sole Dirac component for neutrinos **find CIT**.

0.3.2 Towards a more fundamental theory: GUTs

Despite its highly predictive power, a number of conceptual issues arise in the SM which disfavor it to be a good candidate for a fundamental theory.

The SM does not include a suitable dark matter candidate and a mechanisms that accounts for the baryon asymmetry of the universe. Additionally, up to a total of 25 parameters remain seemingly arbitrary and need to be fitted to data: 3 gauge couplings, 9 charged fermion masses, 3 mixing angles and one CP phase in the CKM matrix, the Higgs mass and quartic coupling, θ_{QCD} , 3 neutrino mixing angles, 1 Dirac phase and, eventually, 2 Majorana phases.

From a group theory perspective, the SM has a rather complex group structure, where a gauge group is formed with the direct product of other three groups as shown in eq. 1. **Drawing a parallel with the electroweak symmetry breaking mechanism, where the $SU(2)_T \otimes U(1)_Y$ is recovered from $U(1)_{EM}$, an interesting line of simplification for the SM group structure would be to devise a similar mechanism where $SU(3)_C \otimes SU(2)_T \otimes U(1)_Y$ is recovered from an hypothetical larger group. IS THIS CORRECT?** Just as the electroweak unification becomes evident at energies higher than the Higgs VEV, a direct manifestation of Grand Unification Theories (GUTs) would occur at even higher energies.

As the smallness of neutrino masses suggests the existence of a higher mass scale, an other, even stronger, hint to Grand Unification comes from the slope of running of the coupling constants. The coupling constants for the electromagnetic, weak and

strong interactions in the SM vary as a function of the interaction energy as shown in figure 2; they cannot exactly meet under the current experimental constraints, but their trend is interesting enough to push for the construction of theories where perfect unification is achieved through the addition of new particles.

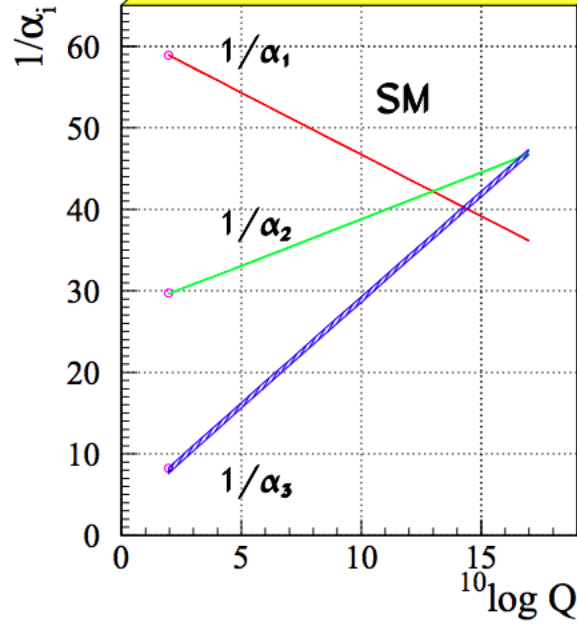


Figure 2: Evolution of the inverse of the three coupling constants in the Standard Model as a function of the momentum transferred, [?].

SU(5). The smallest simple group containing $SU(3)_C \otimes SU(2)_T \otimes U(1)_Y$ is SU(5), as shown first by Georgi and Glashow in [?]. Quarks and leptons in this group fit the $\bar{5}$ and 10 representations. The representation for left-handed fermions are the following

$$\bar{5} = (\nu_e, e^-)_L + \bar{d}_L \quad (13)$$

$$10 = e_L^+ + \bar{u}_L + (u, d)_L, \quad (14)$$

while the boson structure gains a new couple of super heavy bosons (X,Y)

$$24 = \underbrace{(8, 1)}_{\text{gluons}} + \underbrace{(1, 3) + (1, 1)}_{W^\pm, Z, \gamma} + \underbrace{(3, 2) + (\bar{3}, 2)}_{X, Y \text{ bosons}}. \quad (15)$$

Nice features such as charge quantization and the identity between the positron and proton charge value come directly from the group structure. The new super heavy bosons are colored and form a weak doublet. Their are the mediator of the interaction that turns quarks into leptons, leading to predict the existence of processes that violate baryon number, such as $p \rightarrow \pi^0 + e^+$ (see fig 8, right). The prediction for proton decay lifetime, $\tau_p \sim \frac{M_X^4}{m_p^5} \sim 10^{30 \pm 1.5}$ years, is unfortunately experimentally disproved by IMB and Super-K [?].

SO(10). More complicated group structures, such as SO(10) are still viable candidates for GUT. SO(10) includes the same type of X and Y bosons as SU(5). Right-handed massive neutrinos are embedded in the construction of the irreducible representation of SO(10). Different patterns of SO(10) symmetry breaking to recover the SM are possible and lead to different predictions for the proton decay lifetime; some of these predictions are not excluded by the experiments [?].

SUSY GUTs. Supersymmetry theories allow for another family of GUTs [?]. In SUSY, every fundamental particle in the SM has a “superpartner”, identical in each quantum number except for the spin-statistics: the fermion supersymmetric partners are bosons and vice versa. Collider experiments (mainly LHC) constrain the mass of the supersymmetric partners to be very heavy [?]. The SU(5), SU(10) groups with a SUSY twist are the basic groups for SUSY GUTs. From the phenomenology point of view, SUSY models tend to push the proton decay life time higher by a factor of four, they solve the “hierarchy problem”, and they also predict new channels for the proton decay. In particular they predict the presence of kaons in the final product, with a dominant mode of $p \rightarrow \bar{\nu} K^+$. Predictions on the proton decay lifetime depend

on the chosen SUSY model; again, some of the predictions are not excluded by the experiments [?].

0.4 Motivations for Hadronic Cross Sections in Argon

Critical challenges await the next decade of experimental physics at the intensity frontier. Following the recommendation of the latest Particle Physics Project Prioritization Panel [?], the US is dedicating substantial resources to the development of a short- and long- baseline neutrino program to address many of open questions in neutrino physics today. This program pivots on the Liquid Argon Time Projection Chamber (LArTPC) detector technology which will be described in Chapter 1.

The main goals of these research programs include:

- Assessment of the existence of right-handed sterile neutrinos.
- Determination of the sign of Δm_{13}^2 (or Δm_{23}^2), i.e., the neutrino mass hierarchy.
- Determination of the octant, i.e. whether θ_{23} is maximal.
- Determination the status of CP symmetry in the lepton sector.
- Search for observables predicted by GUTs, such as proton decay.

0.4.1 Pion-Argon Total Hadronic Cross Section

This section outlines the importance of the pion-argon total hadronic cross section. We start by discussing the measurement in the context of neutrino interaction searches. We then describe the signal signature and historical measurements of pion-nucleus cross section, as well as the implementation of this cross sections in the current version of the simulation package used by LArIAT.

π^- Ar Cross Section in the Context of Neutrino Searches

As outlined in 0.2.3, neutrino experiments use the products of neutrino interactions to identify the energy and flavor of the incoming neutrino. Pions are a common product of neutrino interaction, especially in resonant scattering, DIS and coherent pion production. For neutrino experiments in argon, there are two main reasons why understanding pion hadronic interactions with argon is important: to model the behavior of the pion inside the nucleus struck by the neutrino and to model the behavior of the pion during its propagation inside the detector medium.

Assumptions on the nuclear models and on the interaction of hadrons inside the nucleus performed at the level of the neutrino event generator bridge the measurement of the products of a neutrino interaction to the reconstruction of the neutrino energy and flavor. Thus, understanding pion hadronic interactions with the nucleus is particularly important to model correctly resonant, DIS and coherent pion production in neutrino interactions, where the presence of pions in the nucleus is abundant. For example, in case of resonant scattering,

$$\nu_l + N \rightarrow l + \Delta/N^* \rightarrow l + \pi + N', \quad (16)$$

the Δ and N^* and excited states will decay hadronically in matters of $\sim 10^{-24}$ s inside the nucleus producing pions which will bounce within the nuclear medium. The decay modes for the lower mass Δ (1232) and N^* (1440) are listed in table 3.

The key elements of a neutrino event generators for resonance and DIS events are the nuclear model and the hadron treatment (both production and transportation). As one of the most popular event generators for LAr experiments, we take GENIE [?] here as an example. The nuclear model used by GENIE for all processes is a relativistic Fermi gas (RFG) modified to incorporate short range nucleon-nucleon correlations [?]. This means that the initial momentum and binding energy of the

struck nucleon is determined by assuming nucleons inside the nucleus are quasi-free, acting independently in the mean field of the nucleus. For $A > 20$ like argon, the 2-parameter Woods-Saxon shell model for density function is used. The GENIE module INTRANUKE [?] is used to simulate the final-state interactions (FSI) which is the hadron re-interaction inside the nucleus. This module places the outgoing particles in the nucleus and propagates them using the “hA model”. In the INTRANUKE hA model, hadrons can undergo at most one FSI per event. When possible, external hadron-nucleus scattering data are used to tune INTRANUKE. Since no data is available for Argon, GENIE uses an interpolation of data from heavier and lighter nuclei for the pion-argon cross section leading to big uncertainties in the INTRANUKE module.

Once the pion has left the target nucleus, the pion-argon hadronic cross section plays an important role in the pion transportation inside the argon medium: processes like pion absorption with emission of nucleons or pion charge exchange can greatly modify the topology of a neutrino interactions in the detector and lead to errors in the event classification. Being able to reconstruct the details of pions inside the detector is an imperative for modern liquid argon neutrino experiment to achieve the design resolution for their key physics measurements.

Signal Signatures

Strong hadronic interaction models [?, ?] predict the pion interaction processes with argon in the [100 - 1200] MeV energy range. The total hadronic π^- -Ar interaction cross section is defined as the one related to the single process driven only by the strong interaction which is dominant in the considered energy range. In measuring the “total” cross section, we include both the elastic and reaction channels, regardless of the final state,

$$\sigma_{Tot} = \sigma_{Elastic} + \sigma_{Reaction}; \quad (17)$$

the reaction channel is further characterizes by several exclusive channels with defined topologies,

$$\sigma_{Reaction} = \sigma_{Inelastic} + \sigma_{abs} + \sigma_{chex} + \sigma_{\pi prod}. \quad (18)$$

A summary of the pion final states in order of pion multiplicity is given in table 4. Pion capture and pion decay at rest dominate the cross section under 100 MeV. We define pion capture as the process determining the formation of a pionic atom and the subsequent pion's end of life. Stopping negative pions can form pionic argon, where the negative pion plays the role of an orbital electron. Since the pion mass is two orders of magnitude greater than the electron mass, the spatial wave form of the pion will overlap way more with the nucleus compared to the electron case. After the electromagnetic formation of the pionic atom, the pion will quickly absorbed by the nucleus, which is put in an excited state. The nucleus then de-excites with the emission of low energy nucleons and photons. Pion capture is predominant compared to pion decay, the other important process for very low energy pions. The decay of a pion is governed by the weak force; the pion decay life time is $\tau_{\pi} = 2.6 \times 10^{-8}$ s and the main decay mode is $\pi^{-} \rightarrow \mu^{-} + \bar{\nu}_{\mu}$ (BR 99.98%). Since pion capture can be considered an electromagnetic process and pion decay is a weak process, this energy region is purposely excluded from the hadronic cross section measurement.

Previous measurements: Lighter and Heavier Nuclei

Many experiments with pion beams have studied the hadronic interaction of pions on light and heavy materials, such as He, Li, C, Fe, Pb [?]. However, data on argon are rare: the total differential hadronic cross section has never been measured before on argon. Simulation packages like Geant4 base their pion transportation for argon on data from lighter and heavier nuclei: the goal of LArIAT's dedicated measurement on argon is to bridge this gap in data, thus reducing the uncertainties related to pions interaction in argon in both neutrino event generators and in simulation packages of

pion transportation.

The shape of the pion-nucleus interaction cross section in the energy range considered shows the distinct features that indicate the presence of a resonance. In fact, the mean free path of a pion of kinetic energy between 100 and 400 MeV is much shorter than the average distance between nucleons (which is of the order of 1 fm). Therefore, the pion interacts with surface nucleons. A Δ resonance is often produced in the interaction, which subsequently decays inside the nucleus. Experimental results on several nuclei as reported in [?] are shown in Figure 3; it is interesting to notice here how the shape of the Δ resonance become less pronounced as a function of the mass number of the target nucleus. Pion interactions with heavier nuclei also shift the peak of the resonance at lower energy; this effect is due to kinematic considerations and to the difference in propagation of the Δ inside the nucleus. Multiple scattering effect modify the resonance width, which is larger than the natural-decay width. As an example of a fairly well studied target, Figure 4 reports the negative pion cross section on Carbon for the elastic and reaction² channels, and their sum [?].

Negative Pion Interaction Cross Section in Generators

LArIAT uses Geant4 as the default simulation package. In particular, pions (and kaons) transportation is achieved through the Geant4 FTFP_BERT physics list. In this physics list, Geant4 uses the Bertini cascade model [?] to simulate the products of the pion-nucleus interaction as well as the secondary hadrons re-interactions inside the target nucleus (intra-nuclear cascade). The target nucleus is represented as a continuous gas where the nuclear potential follows concentric shells whose depths approximate the Woods-Saxon shape. The CERN-HERA compilations [?, ?] of hadron-nucleon interaction data is the data base used for the decision making process after the cascade is invoked. The cross section model determines if the pion

2. What we refer as to “reaction channel” is called “inelastic” in the paper.

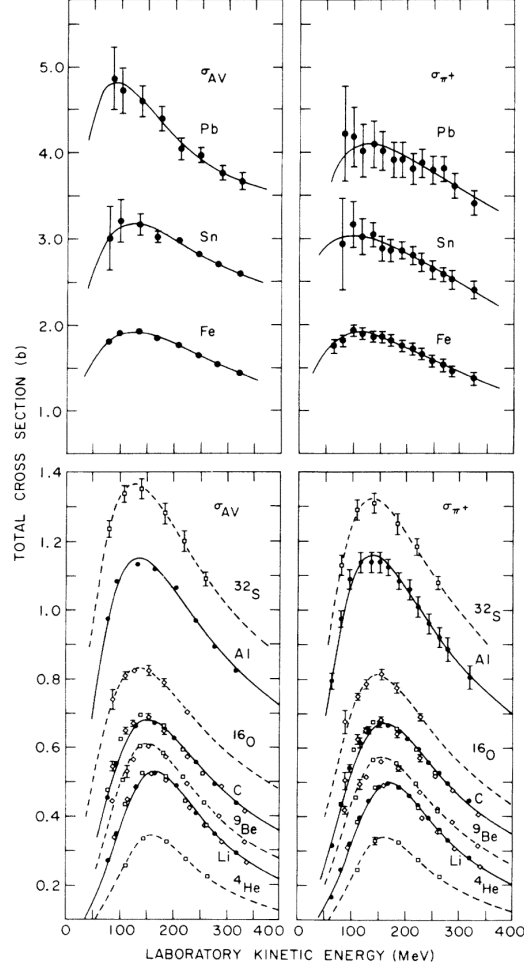


Figure 3: Pion-nucleus total cross sections: σ_{π^+} for positive pions (right) and σ_{AV} (left) for the average between positive and negative pions $\sigma_{AV} = \frac{\sigma_{\pi^+} + \sigma_{\pi^-}}{2}$ in the Δ resonance region. The error bars include estimates of systematic uncertainties. The curves are the results of fits to the data assuming a Breit-Wigner shape. This summary plot is reported in [?] and uses data from [?, ?].

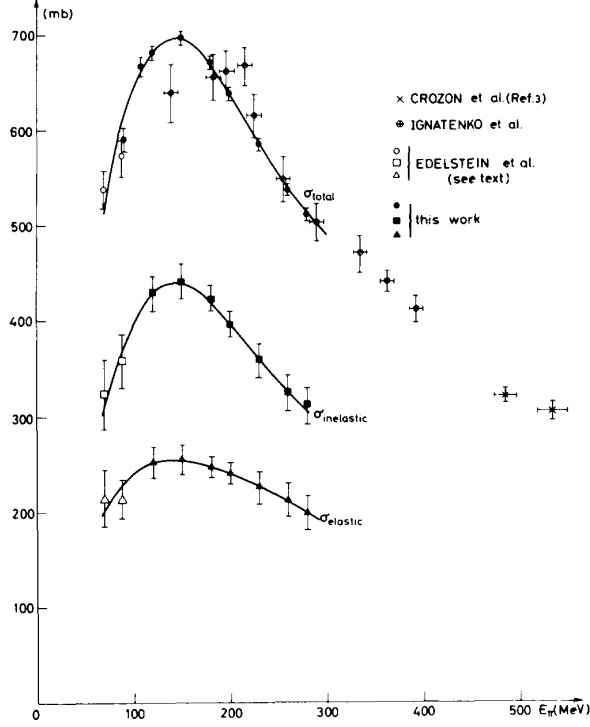


Figure 4: Negative pion nucleus total, elastic and reaction cross sections on ^{12}C as from [?].

interacts, the eventual type of interaction and the interaction multiplicity. For hadron projectiles with energy less than 20 GeV, Geant4 reports the uncertainty on the cross section model to be about the size of the error bars on the data used, or about 10%, increasing to 20-30% in energy regions where data is sparse.

The relevance of the GENIE generator for neutrino physics and its basic working principles have been outlined earlier in this section. Given GENIE's modularity, information on hadron-nucleus interactions can be extracted from the INTRANUKE module and directly compared against the Geant4 predictions.

The work in [?] Irene reviews the current status of negative and positive pion simulation in Geant4 and GENIE for ^{12}C , ^{56}Fe , and ^{40}Ca . From that work, we report the results for ^{12}C in Figure 5 as it allows a direct comparison between Geant4, GENIE and data. Geant4 predictions for π^- on Carbon are in good agreement with data over all the spectrum, while GENIE predictions seem to show some features at

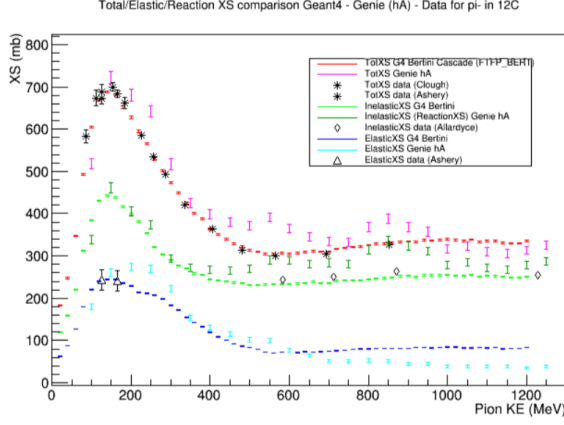


Figure 5: Total, elastic and reaction cross section for π^- on ^{12}C . Comparison between results from Geant4 simulation (Bertini cascade model), Genie simulation (hA model), and experimental data [?, ?, ?, ?].

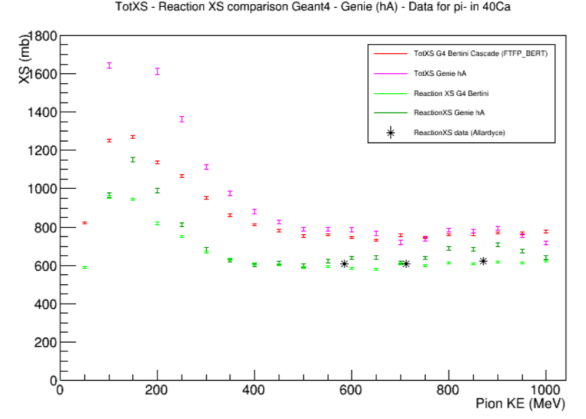


Figure 6: Total, elastic and reaction cross section for π^- on ^{40}Ca . Comparison between results from Geant4 simulation (Bertini cascade model), Genie simulation (hA model), and experimental data [?].

around 500 MeV and 900 MeV, maybe due to higher resonances in the hA model. From the same work, we also report the negative pion cross section on ^{40}Ca in Figure 6, since this is the nuclear medium closest to argon with some available data. The predictions from both Geant4 and GENIE agree with data in the high energy region. The predictions diverge in the resonance region, where data is not available.

For the π^- argon total cross section measurement, we use the Geant4 Bertini Cascade model, whose predictions for the total, elastic and reaction cross sections are shown in Figure 7.

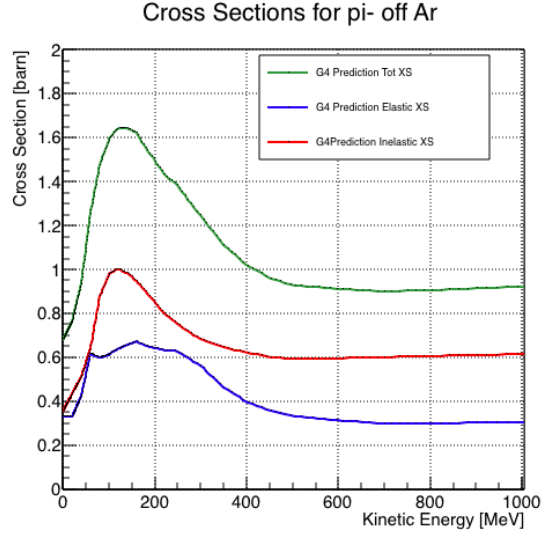


Figure 7: Total, elastic and reaction hadronic cross section for π^- -argon implemented in Geant4 10.01.p3.

Resonance	Decay Mode	Lifetime (s)
$\Delta (1232) 3/2^+$	$\Delta^{++}(uuu) \rightarrow p\pi^+$ $\Delta^+(uud) \rightarrow n\pi^+$ $\Delta^+(uud) \rightarrow p\pi^0$ $\Delta^0(udd) \rightarrow n\pi^0$ $\Delta^0(udd) \rightarrow p\pi^-$ $\Delta^-(ddd) \rightarrow n\pi^-$	$\sim 5.6 \times 10^{-24}$
$N^* (1440) 1/2^+$	$N^* \rightarrow N\pi$ $N^* \rightarrow N\pi\pi$	$\sim 2.2 \times 10^{-24}$

Table 3: Main decay modes of the lightest Delta resonance and Nucleon excited state.

N π in FS	Channel Name	Reaction	Notes
0	Pion Absorption , σ_{abs}	$\pi^-(np) \rightarrow nn$ (2-body abs) $\pi^-(nnp) \rightarrow nnn$ (3-body abs) $\pi^-(npp) \rightarrow pnn$ (3-body abs) $\pi^-(nppp) \rightarrow pnn$ (Multi-body abs)	Suppressed on single nucleon by energy conservation: the process occurs on at least two nucleons system.
1	Elastic Scattering , σ_{el}	$\pi^- + N \rightarrow \pi^- + N$	Scattering on nucleon or nucleus, the target is left in ground state
1	Charge Exchange , σ_{chex}	$\pi^- + p \rightarrow \Delta^0 \rightarrow \pi^0 + n$ $\pi^- + N \rightarrow \pi^+ + \text{nucleons}$	Single charge exchange: charged pion converts into neutral pion Double charge exchange: charged pion converts into opposite charge pion
1	Inelastic Scattering , σ_{inel}	$\pi^- + p \rightarrow \Delta^0 \rightarrow \pi^- + p$ (knock-out) $\pi^- + n \rightarrow \Delta^- \rightarrow \pi^- + n$ (knock-out)	Other possible reactions: Pure Inelastic scattering: population of low energy bound excited states Nuclear break-up with nucleons or fragments knock-out
2+	Pion Production , $\sigma_{\pi prod}$	$\pi^- + N \rightarrow \geq 2\pi + \text{nucleons}$	Possible if pion K.E ≥ 500 Mev/c

Table 4: Summary of negative pion hadronic interactions as a function of the pion multiplicity in the final state in the energy range [100-1200] MeV.

0.4.2 Kaon-Argon Total Hadronic Cross Section

This section outlines the importance of the kaon-argon total hadronic cross section. We start by discussing the measurement in the context of nucleon decay searches. We then describe the signal signature and historical measurements of kaon-nucleus cross section, as well as the implementation of this cross sections in the current version of the simulation package used by LArIAT.

K^+Ar Cross section in the Context of Nucleon Decay Searches

Nucleon decay

Baryon number is accidentally conserved in the Standard Model. Even though no baryon number violation has been experimentally observed thus far, no underlying symmetry in line with the Noether paradigm [?] explains its conservation. As shown in section 0.3.2, almost all Grand Unified Theories predict at some level baryon number violation in the form of nucleon decay on long time-scales. Given the impossibility to reach grand unification energy scales with collider experiments ($\sqrt{s} > 10^{15}$ GeV), an indirect proof of GUTs is needed. The experimental observation of nucleon decay may be the only viable way to explore these theories.

In case of nucleon decay discovery, the dominant decay mode may uncover additional information about the GUT type. Supersymmetric GUTs [?, ?] prefer the presence of kaons in the products of the decay, e.g. $p \rightarrow K^+\bar{\nu}$ (see fig 8, left). Gauge mediated GUTs, in which new gauge bosons are introduced that allow for the transformation of quarks into leptons, and vice versa, prefer the mode $p \rightarrow e^+\pi^0$ (see fig 8, right).

LArIAT tiny active volume makes it impossible for the experiment to place competitive limits on nucleon decay searches. However, LArIAT provides excellent data to characterize kaons in liquid argon for the “LAr golden mode”, $p \rightarrow K^+\bar{\nu}$. The

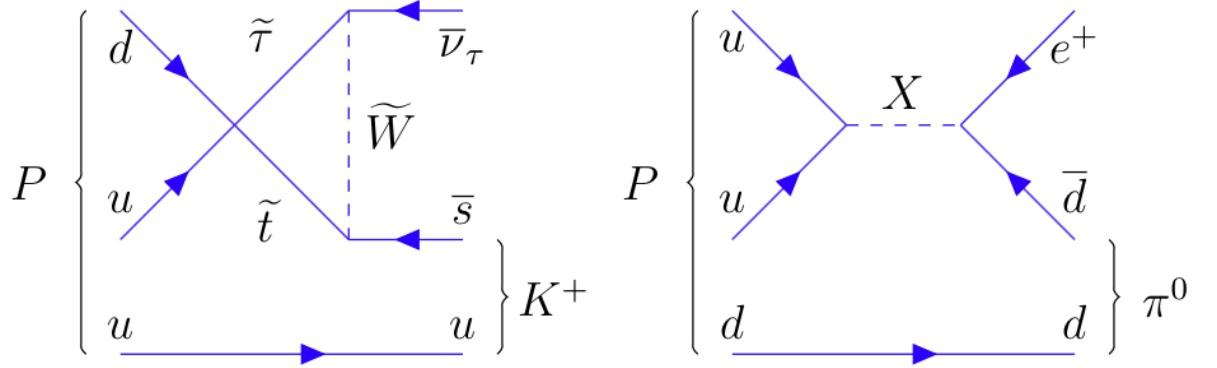


Figure 8: Feynman diagrams for proton decay “golden modes”: $p \rightarrow K^+ \bar{\nu}$ for supersymmetric GUTs on the left and $p \rightarrow e^+ \pi^0$ for gauge-mediated GUTs on the right.

result of these studies will affect future proton decay searches in LArTPCs. Previous work has been done to assess the potential identification efficiency for different decay modes in a LArTPC [?], but, as the time of this writing, no study of kaon selection efficiency in LArTPCs has been performed on data. The K^+ -Ar interaction cross section has never been measured before and can affect the possibility of detecting and measuring kaons when produced in a proton decay event. Kaon interactions with argon can distort the kaon energy spectrum as well as change the topology of single kaon events. In a LArTPC, non-interacting kaons appear as straight tracks with a high ionization depositions at the end (Bragg peak). The topology of interacting kaons can be quite different. In case of elastic scattering, a distinct kink will be present in the track. In case of inelastic scattering the Bragg peak will not be present and additional tracks will populate the event. Performing the total hadronic K^+ -Ar cross section measurement on data serves the double purpose of identifying the rate of “unusual” topologies (kinks and additional tracks) and of developing tools for kaon tracking in LAr.

Signal Signatures

The interaction of a mildly relativistic charged kaon with an argon nucleus is determined largely by the strong force. The total hadronic K^+ -Ar interaction cross section is defined as the one related to the single (hadronic) process driven only by the strong interaction. In this case, “total” indicates all strong interactions regardless of the final state. This condition purposefully includes both elastic and inelastic (reaction) channels. Indeed, the total cross section can be then decomposed into

$$\sigma_{Tot} = \sigma_{Elastic} + \sigma_{Reaction}.$$

For the LArIAT cross section analysis, the kaons considered span a momentum inside the TPC from 100 MeV/c to 800 MeV/c. In this energy range, the relevant K-Nucleon interactions are according to [?]:

$$K^+ + N \rightarrow K^+ + N \text{ (elastic)} \tag{19}$$

$$K^+ + n \rightarrow K^0 + p \text{ (elastic)} \tag{20}$$

$$K^+ + N \rightarrow K + N + \pi \text{ (inelastic)} \tag{21}$$

$$K^+ + N \rightarrow K^* + N \text{ (inelastic)}. \tag{22}$$

Previous Measurements: Lighter and Heavier Nuclei

In general, measurements on kaon cross sections are extremely scarce. The measurement of the kaon interaction cross section would bring the additional benefit of reducing the uncertainties associated with hadron interaction models adopted in MC simulations for argon targets, beneficial for both proton decay studies and kaon production from neutrino interaction studies, where the uncertainties for final state interaction models are big [?].

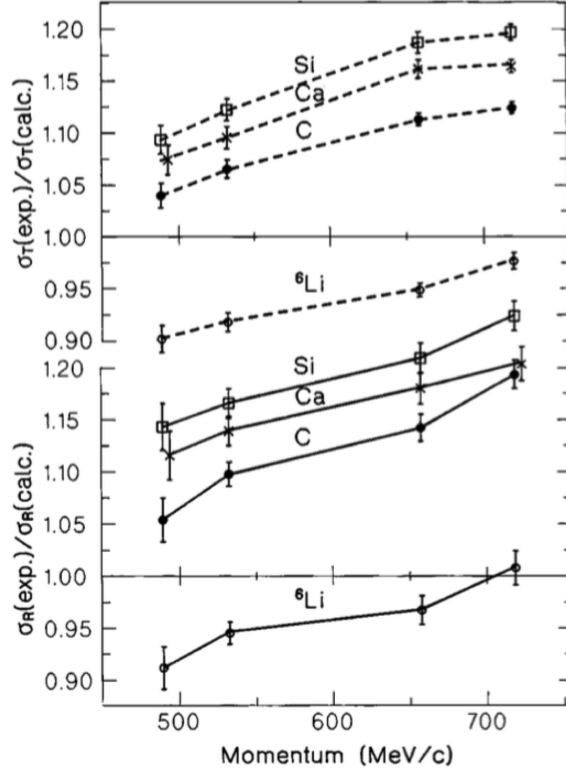


Figure 9: Ratios between experimental and calculated cross sections as from [?]. Top: Total cross sections. Bottom: reaction cross sections.

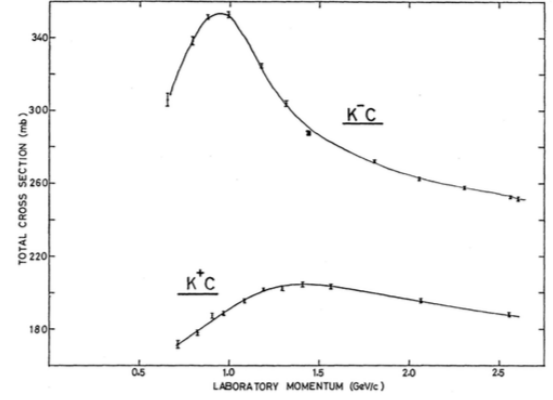


Figure 10: Total K^+ and K^- cross sections on carbon as from [?].

Figure 9 shows a 1997 measurement on several elements as performed by Friedmann et al. [?]. As a reference, this paper measures a σ_{Tot} for Si of 366.5 ± 4.8 mb and a σ_{Tot} for Ca of 494.6 ± 7.7 mb at 488 MeV/c. The cross section for argon is expected to lie in between these two measurements. Additional data on the kaon cross section are provided by Bugg et al. [?]. Bugg performs a measurement of the total K^+ and K^- cross sections on protons and deuterons over the range of 0.6-2.65 GeV/c, as well as a measurement of the total K^+ and K^- cross sections on carbon for a number of momenta; the results of this paper on carbon are reported in Figure 10.

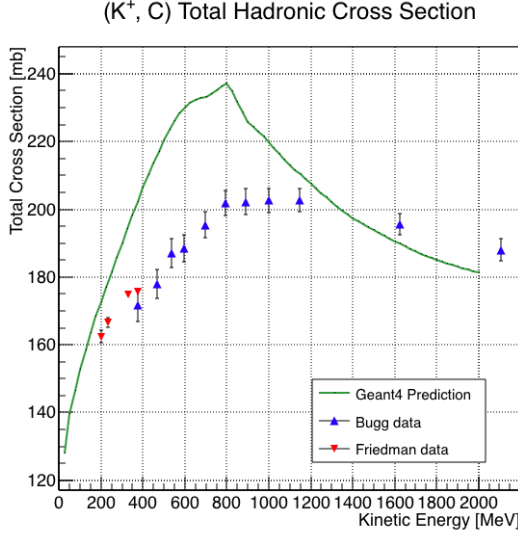


Figure 11: Total hadronic cross section for carbon implemented in Geant4 10.01.p3 with overlaid with the Bugg and Frideman data.

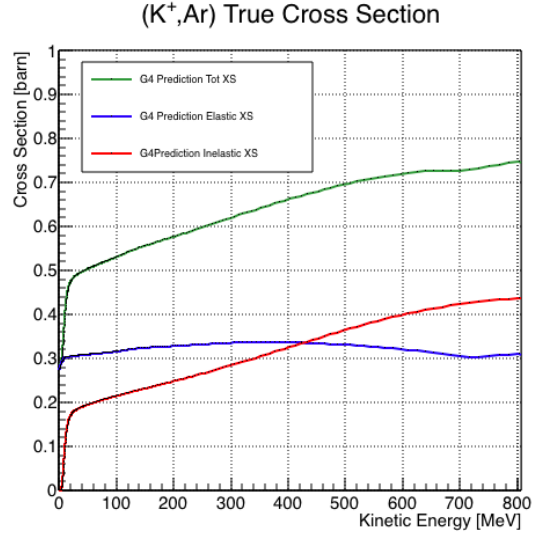


Figure 12: Total, elastic and reaction hadronic cross section for K^+ -argon implemented in Geant4 10.01.p3.

Kaon Interaction Cross Section for thin target in Geant4

Since the kaon cross section in argon has never been measured before, simulation packages tune kaon transportation in argon by extrapolation from lighter and heavier nuclei. LArIAT uses the Geant4 suite for particle transportation. Since kaon data on carbon are available, we used it as a metric to evaluate the Geant4 prediction performances. Figure 11 shows the total hadronic cross section for carbon implemented in Geant4 10.01.p3 overlaid with the Bugg and Friedman data. Unfortunately, the current version of Geant4 does not reproduce the data for carbon closely. On one hand, this evidence makes us even more wary when using the Monte Carlo in simulating the kaon-argon interactions. On the other, it further highlights the importance of the kaon measurement. Figure 12 shows the Geant4 prediction for the total, elastic and reaction cross section for K^+ on argon.

Chapter 1

Liquid Argon Detectors at the Intensity Frontier

In the next few years, LArTPC experiments – such as the Short-Baseline Neutrino program (SBN) and DUNE – will be the tools to answer some of the burning questions in neutrino physics today. This section illustrates the operational principles of this detector technology, as well as the scope of SBN, DUNE and LArIAT in the current intensity frontier panorama.

1.1 The Liquid Argon Time Projection Chamber Technology

1.1.1 Time Projection Chamber

1.1.2 LArTPC: Principles of Operation

To the bare bones, a LArTPC is a bulk of liquid argon sandwiched in a flat capacitor, equipped with a light collection system. A uniform electric field of the order of 500 V/cm is maintained constant between the faces of the capacitor. The anode is

sensitive to ionization charge and it is usually made of two or more planes segmented into several hundreds parallel sense wires a few millimeters apart; different geometries for the anode segmentation are under study [2].

Argon ionization and scintillation are the processes leveraged to detect particles in the LArTPC active volume. When a ionizing radiation traverses the argon active volume it leaves a trail of ionization electrons along its trajectory and it excites the argon, leading to the production of scintillation light – details on the production and detection of ionization charge and scintillation light are provided in 1.1.4 and 1.1.4 respectively. The optical part of the detector collects the argon scintillation light in matters of nanoseconds. This flash of light determines the start time of an event in the chamber, t_0 . The uniform electric field drifts the ionization electrons from the production point towards the anode plane in order of hundreds of microseconds or more depending on the chamber dimensions¹. The anode sense wires see either an induced current by the drifting charge (on induction planes) or an injection of the ionization charge (collection plane) [94]. An appropriate choice of the voltage bias on each wire plane assures ideal charge transparency, so that all the ionization charge is collected on the collection plane and none on the induction planes [95].

The arrival time of the charge on the anode sense wires is used to measure the position of the original ionizing radiation in the drift direction. In fact, since the constant electric field implies that the drift velocity is also constant in the chamber, the position of the original ionization is simply given by the multiplication of the drift velocity by the drift time, where we define as “drift time” the difference between t_0 and the charge arrival time on the wire planes. The spacial resolution on this dimension is limited by the time resolution of the electronics or by longitudinal diffusion of the

1. The ionized argon also drifts, but in the opposite directions compared to the electrons. Since the drift time is proportional to the particle mass, the ions drift time is much longer than the electrons’. Ionized argon is collected on the cathode which is not instrumented, so it is not used to infer information about the interactions in the chamber.

electrons. The spatial information on the different wire planes maps a bi-dimensional projection of the interaction pattern in the plane perpendicular to the drift direction. The spacial resolution on this dimension is limited by the transverse electron diffusion in argon and by the grain of the anode segmentation, i.e. the spacing between the wires in the sense planes [100]. The off-line combination of the 2-D information on the wire planes with the timing information allows for the 3D reconstruction of the event in the chamber.

Calorimetry

1.1.3 Liquid Argon: Ionization Charge

Electron Life Time & purity

LArTPCs use hermetically sealed and leak-checked vessels to abate the leakage and diffusion of contaminants into the system. The liquid argon filling of the volume occurs after the vessel is evacuated or purged with gaseous argon [205] to reduce remaining gases in the volume. Even so, the construction of a pure tank of argon is unviable, as several sources of impurity remain. In particular, impurities can come from the raw argon supply, the argon filtration system and from the outgassing from internal surfaces. Outgassing is a continuous diffusive process producing contaminants, especially water, even after the vessel is sealed, particularly from materials in the ullage region². Since research-grade argon comes from the industrial distillation of air, the impurities with the highest concentration are nitrogen, oxygen and water, generally maintained under the 1 part per million level by the vendor. Even so, a higher level of purity is necessary to achieve a free electron life time usable in meter scale detectors. Thus, argon is constantly filtered in the cryogenic system, which reduce the oxygen and water contamination to less than 100 parts per trillion. The

² . While the liquid argon low temperature reduces outgassing in the liquid, this process remains significant for absorptive material (such as plastic) above the surface of the liquid phase

filtration system depends on the size and drift distance of the experiment and, for experiments on several meters scale, it includes an argon recirculation system.

Space Charge Effect

Recombination Effect

1.1.4 Liquid Argon: Scintillation Light

Liquid argon emits scintillation light at the passage of charged particles. LArTPCs leverage this property to determine when the ionization charge begins to drift towards the anode plane.

Scintillation Process

Scintillation light in argon peaks in the ultraviolet at a 128 nm, shown in comparison to Xenon and Krypton in Figure [183]. The light yield collected by the optical detector depends on the argon purity, the electric field, the dE/dx and particle type, averaging at the tens of thousands of photons per MeV. The de-excitation of Rydberg dimers in the argon is responsible for the scintillation light. Rydberg dimers exist in two states: singlets and triplets. The time constant for the singlet radiative decay is 6 ns, resulting in a prompt component for the scintillation light. The decay of the triplet is delayed by intersystem crossing, producing a slow component with a time constant of ~ 1500 ns. “Self-trapped exciton luminescence” and “recombination luminescence” are the two processes responsible for the creation of the Rydberg dimers. In the first process, a charged particle excites an argon atom which becomes self-trapped in the surrounding bulk of argon, forming a dimer; the dimer is in the singlet state 65% of the times and in the triplet state 35% of the times. In case of recombination luminescence, the charged particle transfers enough energy to ionize the argon. The argon ion forms a charged argon dimer state, which quickly recombines with the

thermalized free electron cloud. Excimer states are produced in the recombination, roughly half in the singlet and half in the triplet state. The light yield dependency on the electric field, on the dE/dx and particle type derives from the role of free charge in the recombination luminescence process. The spacial separation between the argon ions and the free electron cloud depends on the electric field. On one hand, a strong electric field diminishes the recombination probability, leading to a smaller light yield; on the other, it increases the free charge drifting towards the anode plane. Hence, the amount of measurable charge and light anti-correlates as a function of the electric field. Ionizing particles in the argon modify the local density of both free electrons and ions depending on their dE/dx . Since the recombination rate is proportional to the square of the local ionization density, highly ionizing particles boost recombination and the subsequent light yield compared to MIPs. The possibility to leverage this dependency for pulshape-based particle identification has been shown in [186], [187].

Effects Modifying the Light Yield

The production mechanism through emission from bound excimer states implies that argon is transparent to its own scintillation light. In fact, the photons emitted from these metastable states are not energetic enough to re-excite the argon bulk, greatly suppressing absorption mechanisms. In a LArTPC however, several processes modify the light yield in between the location where light is produced and the optical detector. In a hypothetical pure tank of argon, Rayleigh scattering would be the most important processes modifying the light yield. Rayleigh scattering changes the path of light propagation in argon, prolonging the time between light production and detection. The scattering length has been measured to be 66 cm [191], shorter than the theoretical prediction of ~ 90 cm [190]; this value is short enough to be relevant for the current size of LArTPCs detectors. In fact, Rayleigh scattering worsen the resolution on t_0 , the start time for charge drifting, and alters the light directionality,

complicating the matching between light and charge coming from the same object in case of multiple charged particles in the detector.

Traces of impurities in argon such as oxygen, water and nitrogen also affect the light yield, mainly via absorption and quenching mechanisms. Absorption occurs as the interaction of a 128 nm photon directly with the impurity dissolved in the liquid argon. Differently, quenching occurs as the interaction of an argon excimer and an impurity, where the excimer transfers its excitation to the impurity and dissociates non-radiatively. Given this mechanism, it is evident how quenching is both a function of the impurity concentrations and the excimer lifetime. Since the triplet states live much longer than the singlet states, quenching occurs mainly on triplet states, affecting primarily the slow component of the light, reducing the scintillation yield and a shortening of the scintillation time constants.

The stringent constraints for the electron life time limit the presence of oxygen and water to such a low level that both absorption and quenching on these impurity is not expected to be significant [210]. Contrarily, the nitrogen level is not bound by the electron life time constraints – nitrogen being an inert gas, expensive to filter. Thus, nitrogen is often present at the level provided by the vendor. The effects of nitrogen on argon scintillation light have been studied in the WArP R&D program and at several test stands. The quenching process induced by nitrogen in liquid Ar has been measured to be proportional to the nitrogen concentration, with a rate constant of $\sim 0.11 \mu s^{-1} \text{ ppm}^{-1}$; appreciable decreasing in lifetime and relative amplitude of the slow component have been shown for contamination as high as a few ppm of nitrogen [1]. For a nitrogen concentration of 2 parts per million, typical of the current generation of LArTPC, the attenuation length due to nitrogen has been measured to be ~ 30 meters [4].

Wavelength Shifting of LAr Scintillation Light

Liquid argon scintillation light is invisible for most optical detectors deployed in LArTPC, such as cryogenic PMTs and SiPMs, since a wavelength of 128 nm is generally too short to be absorbed from most in glasses, polymers and semiconductor materials. Research on prototype SiPMs absorbing directly VUV light and their deployment in noble gasses experiment is ongoing but not mature [5]. Thus, experiments need to shift the wavelength of scintillation light to be able to detect it. Albeit deployed in different ways, neutrinos and dark matter experiments commonly use 1,1,4,4-tetraphenyl-butadiene (TPB) to shift the scintillation light. TPB, whose chemical structure is shown in figure , absorbs the vacuum ultraviolet (VUV) light and emits in the visible at ~ 425 nm [231], with a ratio of visible photon emitted per VUV photon absorbed of $\sim 1.2:1$ [3].

Neutrino experiments typically coat their optical detector system evaporating a layer of TPB either directly on the PMTs glass surface or on acrylic plates mounted in front of the PMTs [cite microboone](#); this technique allows the fast detection light coming directly from the neutrino interaction. Dark matter experiments typically evaporate TPB on reflective foils mounted on the inside walls of the sensitive volume and detect the light after it has been reflected; this technique leads to a higher and more uniform light yield, though scattering effects for both the visible and VUV light augment the propagation time and hinder directionality information [some DM detector](#) . In order to take advantage of both these techniques, hybrid systems with PMT coating and foils are being considered for the next generation of large neutrino detectors [cite SBND?](#).

1.1.5 Signal processing

1.2 The Intensity Frontier Program

1.2.1 SBN: Neutrino Interaction and Detection

1.2.2 DUNE: Rare Decay Searches

The key elements for a rare decay experiment are: massive active volume, long exposure, high identification efficiency and low background. Figure 1.1 shows the current best experimental limits on nucleon decay lifetime over branching ratio (dots). Historically, the dominant technology used in these searches has been water Cherenkov detectors: all the best experimental limits on every decay mode are indeed set by Super-Kamiokande [?, ?]. It is particularly important to notice that the kaon energy for the proton decay mode $p \rightarrow K^+ \bar{\nu}$ is under Cherenkov threshold. Super-Kamiokande set the limit on the lifetime for the $p \rightarrow K^+ \bar{\nu}$ mode by relying exclusively on photons from nuclear de-excitation. For this reason, an attractive alternative approach to identifying nucleon decay is the use of a Liquid Argon Time Projection Chamber (LArTPC).

LArTPCs can complement nucleon decay searches in modes where water Cherenkov detectors are less sensitive, especially $p \rightarrow K^+ \bar{\nu}$. According to [?], DUNE will have an active volume large enough, have sufficient shielding from the surface, and will run for lengths of time sufficient to compete with Hyper-K, opening up the opportunity for the discovery of nucleon decay.

1.2.3 Enabling the next generation of discoveries: LArIAT

LArIAT, a small Liquid Argon Time Projection Chamber (LArTPC) in a test beam, is designed to perform an extensive physics campaign centered on charged particle

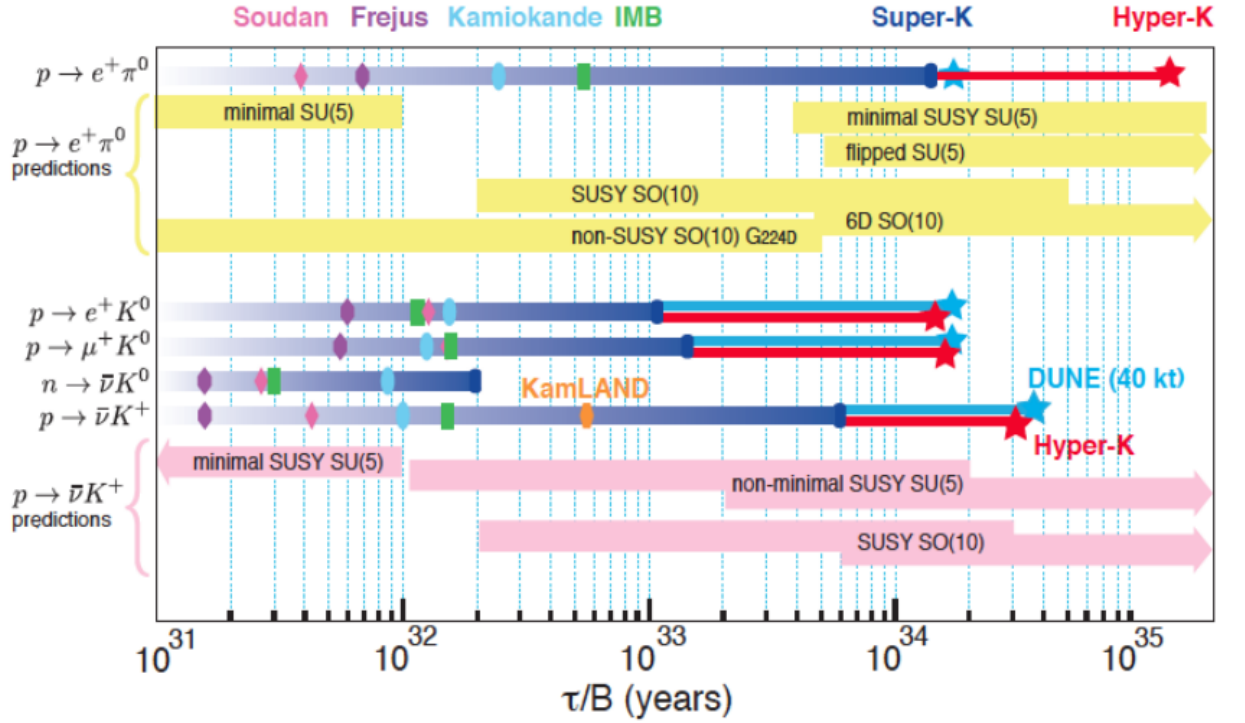


Figure 1.1: Proton decay lifetime limits from passed and future experiments.

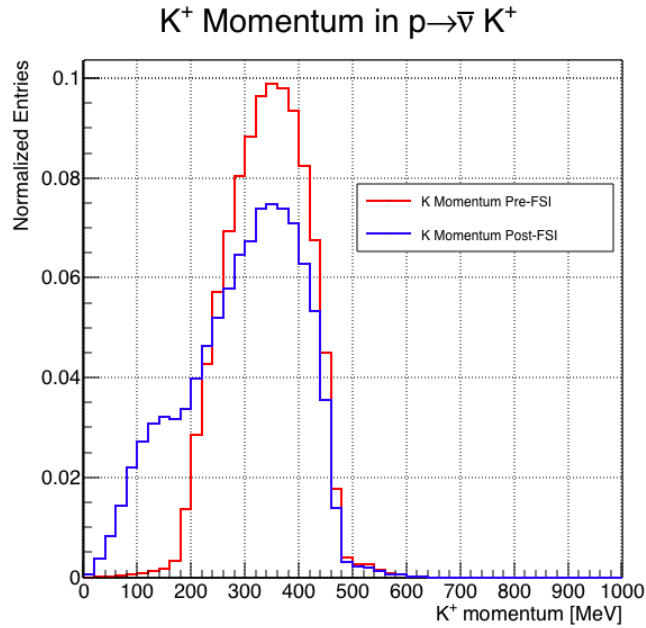


Figure 1.2: Momentum of the kaon outgoing a proton decay event as simulated by the Genie 2.8.10 event generator in argon. The red line represent the kaon momentum distribution before undergoing the simulated final state interaction inside the argon nucleus, while the blue line represents the momentum distribution after FSI.

cross section measurements while characterizing the detector performance for future LArTPCs. LArTPC represents one of the most advanced experimental technologies for physics at the Intensity Frontier due to its full 3D-imaging, excellent particle identification and precise calorimetric energy reconstruction. This complex technology however needs a thorough calibration and dedicated measurements of some key quantities to achieve the precision required for the next generation of discoveries at the Intensity Frontier which LArIAT can provide.

The LArIAT LArTPC is deployed in a dedicated calibration test beamline at Fermilab. We use the LArIAT beamline to characterize the charge particles before they enter the TPC: the particle type and initial momentum is known from beamline information. The precise calorimetric energy reconstruction of the LArTPC technology enables the measurement of the total differential cross section for tagged hadrons. The Pion-Nucleus and Kaon-Nucleus total hadronic interaction cross section have never been measured before in argon and they are a fundamental step to shed light on light meson interaction in nuclei. Additionally, these measures provides a key input to neutrino physics and proton decay studies in future LArTPC experiments like SBN and DUNE. add paragraph on all wonderful things lariat can do... some event displays would be nice!

ADD genie proton decay kaon distribution and lariat beamline overlaid The signature of a proton decay event in the “LAr golden mode” is the presence of a single kaon of about 400 MeV in the detector.

Bibliography

- [1] R Acciarri, M Antonello, B Baibussinov, M Baldo-Ceolin, P Benetti, F Calaprice, E Calligarich, M Cambiaghi, N Canci, F Carbonara, F Cavanna, S Centro, A G Cocco, F Di Pompeo, G Fiorillo, C Galbiati, V Gallo, L Grandi, G Meng, I Modena, C Montanari, O Palamara, L Pandola, G B Piano Mortari, F Pietropaolo, G L Raselli, M Roncadelli, M Rossella, C Rubbia, E Segreto, A M Szelc, S Ventura, and C Vignoli. Effects of nitrogen contamination in liquid argon. *Journal of Instrumentation*, 5(06):P06003, 2010.
- [2] A Ereditato, C C Hsu, S Janos, I Kreslo, M Messina, C Rudolf von Rohr, B Rossi, T Strauss, M S Weber, and M Zeller. Design and operation of argontube: a 5 m long drift liquid argon tpc. *Journal of Instrumentation*, 8(07):P07002, 2013.
- [3] V.M. Gehman, S.R. Seibert, K. Rielage, A. Hime, Y. Sun, D.-M. Mei, J. Maassen, and D. Moore. Fluorescence efficiency and visible re-emission spectrum of tetraphenyl butadiene films at extreme ultraviolet wavelengths. *Nuclear Instruments and Methods in Physics Research Section A: Accelerators, Spectrometers, Detectors and Associated Equipment*, 654(1):116 – 121, 2011.
- [4] B J P Jones, C S Chiu, J M Conrad, C M Ignarra, T Katori, and M Toups. A measurement of the absorption of liquid argon scintillation light by dissolved nitrogen at the part-per-million level. *Journal of Instrumentation*, 8(07):P07011, 2013.

- [5] N Yahlali, L M P Fernandes, K Gonzlez, A N C Garcia, and A Soriano. Imaging with sipms in noble-gas detectors. *Journal of Instrumentation*, 8(01):C01003, 2013.